Astroparticle Physics 48 (2013) 16–24

Contents lists available at SciVerse ScienceDirect

Astroparticle Physics

journal homepage: www.elsevier.com/locate/astropart

The energy spectrum of ultra-high-energy cosmic rays measured by the Telescope Array FADC fluorescence detectors in monocular mode

T. Abu-Zayyad [a], R. Aida [b], M. Allen [a], R. Anderson [a], R. Azuma [c], E. Barcikowski [a], J.W. Belz [a], D.R. Bergman [a], S.A. Blake [a], R. Cady [a], B.G. Cheon [d], J. Chiba [e], M. Chikawa [f], E.J. Cho [d], W.R. Cho [g], H. Fujii [h], T. Fujii [i,*], T. Fukuda [c], M. Fukushima [j,t], W. Hanlon [a], K. Hayashi [c], Y. Hayashi [i], N. Hayashida [l], K. Hibino [l], K. Hiyama [j], K. Honda [b], T. Iguchi [c], D. Ikeda [j], K. Ikuta [b], N. Inoue [m], T. Ishii [b], R. Ishimori [c], H. Ito [u], D. Ivanov [a], S. Iwamoto [b], C.C.H. Jui [a], K. Kadota [o], F. Kakimoto [c], O. Kalashev [k], T. Kanbe [b], K. Kasahara [p], H. Kawai [q], S. Kawakami [i], S. Kawana [m], E. Kido [j], H.B. Kim [d], H.K. Kim [g], J.H. Kim [d], J.H. Kim [a], K. Kitamoto [f], S. Kitamura [c], Y. Kitamura [c], K. Kobayashi [e], Y. Kobayashi [c], Y. Kondo [j], K. Kuramoto [i], V. Kuzmin [k], Y.J. Kwon [g], J. Lan [a], S.I. Lim [s], J.P. Lundquist [a], S. Machida [c], K. Martens [t], T. Matsuda [h], T. Matsuura [c], T. Matsuyama [i], J.N. Matthews [a], I. Myers [a], M. Minamino [i], K. Miyata [e], Y. Murano [c], S. Nagataki [u], T. Nakamura [v], S.W. Nam [s], T. Nonaka [j], S. Ogio [i], J. Ogura [c], M. Ohnishi [j], H. Ohoka [j], K. Oki [j], D. Oku [b], T. Okuda [i], M. Ono [u], A. Oshima [i], S. Ozawa [p], I.H. Park [s], M.S. Pshirkov [w], D.C. Rodriguez [a], S.Y. Roh [r], G. Rubtsov [k], D. Ryu [r], H. Sagawa [j], N. Sakurai [i], A.L. Sampson [a], L.M. Scott [n], P.D. Shah [a], F. Shibata [b], T. Shibata [j], H. Shimodaira [j], B.K. Shin [d], J.I. Shin [g], T. Shirahama [m], J.D. Smith [a], P. Sokolsky [a], T.J. Sonley [a], R.W. Springer [a], B.T. Stokes [a], S.R. Stratton [a,n], T.A. Stroman [a,*], S. Suzuki [h], Y. Takahashi [j], M. Takeda [j], A. Taketa [x], M. Takita [j], Y. Tameda [j], H. Tanaka [i], K. Tanaka [y], M. Tanaka [h], S.B. Thomas [a], G.B. Thomson [a], P. Tinyakov [k,v], I. Tkachev [k], H. Tokuno [c], T. Tomida [b], S. Troitsky [k], Y. Tsunesada [c], K. Tsutsumi [c], Y. Tsuyuguchi [b], Y. Uchihori [z], S. Udo [l], H. Ukai [b], G. Vasiloff [a], Y. Wada [m], T. Wong [a], Y. Yamakawa [j], R. Yamane [i], H. Yamaoka [h], K. Yamazaki [i], J. Yang [s], Y. Yoneda [i], S. Yoshida [q], H. Yoshii [aa], R. Zollinger [a], Z. Zundel [a]

[a] University of Utah, High Energy Astrophysics Institute, Salt Lake City, UT, USA
[b] University of Yamanashi, Interdisciplinary Graduate School of Medicine and Engineering, Kofu, Yamanashi, Japan
[c] Tokyo Institute of Technology, Meguro, Tokyo, Japan
[d] Hanyang University, Seongdong-gu, Seoul, Republic of Korea
[e] Tokyo University of Science, Noda, Chiba, Japan
[f] Kinki University, Higashi Osaka, Osaka, Japan
[g] Yonsei University, Seodaemun-gu, Seoul, Republic of Korea
[h] Institute of Particle and Nuclear Studies, KEK, Tsukuba, Ibaraki, Japan
[i] Osaka City University, Osaka, Japan
[j] Institute for Cosmic Ray Research, University of Tokyo, Kashiwa, Chiba, Japan
[k] Institute for Nuclear Research of the Russian Academy of Sciences, Moscow, Russia
[l] Kanagawa University, Yokohama, Kanagawa, Japan
[m] Saitama University, Saitama, Japan
[n] Rutgers, The State University of New Jersey, Piscataway, NJ, USA
[o] Tokyo City University, Setagaya-ku, Tokyo, Japan
[p] Waseda University, Advanced Research Institute for Science and Engineering, Shinjuku-ku, Tokyo, Japan
[q] Chiba University, Chiba, Japan
[r] Chungnam National University, Yuseong-gu, Daejeon, Republic of Korea
[s] Ewha Womans University, Seodaaemun-gu, Seoul, Republic of Korea
[t] Kavli Institute for the Physics and Mathematics of the Universe (WPI), Todai Institutes for Advanced Study, The University of Tokyo, Kashiwa, Chiba, Japan
[u] RIKEN, Wako, Saitama, Japan
[v] Kochi University, Kochi, Japan
[w] University Libre de Bruxelles, Brussels, Belgium
[x] Earthquake Research Institute, University of Tokyo, Bunkyo-ku, Tokyo, Japan
[y] Hiroshima City University, Hiroshima, Japan
[z] National Institute of Radiological Science, Chiba, Japan
[aa] Ehime University, Matsuyama, Ehime, Japan

* Corresponding author.
E-mail address: tstroman@physics.utah.edu (T.A. Stroma).

0927-6505/$ - see front matter
http://dx.doi.org/10.1016/j.astropartphys.2013.06.007

ARTICLE INFO

Article history:
Received 17 May 2013
Received in revised form 13 June 2013
Accepted 16 June 2013
Available online 27 June 2013

Keywords:
UHECR
Energy spectrum
Fluorescence
Monocular

ABSTRACT

We present a measurement of the energy spectrum of ultra-high-energy cosmic rays performed by the Telescope Array experiment using monocular observations from its two new FADC-based fluorescence detectors. After a short description of the experiment, we describe the data analysis and event reconstruction procedures. Since the aperture of the experiment must be calculated by Monte Carlo simulation, we describe this calculation and the comparisons of simulated and real data used to verify the validity of the aperture calculation. Finally, we present the energy spectrum calculated from the merged monocular data sets of the two FADC-based detectors, and also the combination of this merged spectrum with an independent, previously published monocular spectrum measurement performed by Telescope Array's third fluorescence detector [T. Abu-Zayyad et al., The energy spectrum of Telescope Array's middle drum detector and the direct comparison to the high resolution fly's eye experiment, Astroparticle Physics 39 (2012) 109-119, http://dx.doi.org/10.1016/j.astropartphys.2012.05.012, Available from: <arXiv:1202.5141>]. This combined spectrum corroborates the recently published Telescope Array surface detector spectrum [T. Abu-Zayyad, et al., The cosmic-ray energy spectrum observed with the surface detector of the Telescope Array experiment, ApJ 768 (2013) L1, http://dx.doi.org/10.1088/2041-8205/768/1/L1, Available from: <arXiv:1205.5067>] with independent systematic uncertainties.

1. Introduction

Ultra-high-energy cosmic rays (UHECRs) are charged subatomic particles of extraterrestrial origin with kinetic energies above 10^{18} eV, making them the most energetic particles in the known universe. A clear understanding of their origins and chemical composition has not yet been experimentally established, largely due to the scarcity of UHECRs: collecting enough data to suppress uncertainty from small-number statistics requires a detector that can observe a large area for a long time. The Telescope Array (TA) experiment in western Utah is the largest UHECR detector currently operating in the northern hemisphere[1] [2,3]. Centered at approximately 112.9° W, 39.3° N near the city of Delta in Millard County, TA is a "hybrid" detector consisting of three atmospheric fluorescence detector (FD) stations and a ground array of 507 surface detectors (SDs) on a square grid with 1200-meter spacing (see Fig. 1).

Each of the FDs and the SD array operate independently, collecting data for UHECR measurements. The SDs, which directly detect secondary particles in the extensive air shower produced by a primary UHECR, collect data night and day in all weather and thus have a duty cycle of nearly 100%. The FDs use telescopes to measure ultraviolet light produced when an air shower excites atmospheric N_2. For best sensitivity, FDs operate only on moonless nights, so their duty cycles are each approximately 10%.

Although the SD array alone boasts the strongest statistical power within the experiment, combining and comparing data from different components of TA allows distinct, corroborating measurements of physical quantities of interest. Using the simultaneous observation of a single cosmic-ray air shower by one FD and either the SD array ("hybrid") or a second FD ("stereo"), we tightly constrain certain geometric properties of the air shower, but the majority of UHECRs do not satisfy this observation criterion. The "monocular" observation of UHECRs, reconstructing events using measurements from a single FD station, accumulates data at a rate second only to the SD array, and has several additional advantages over hybrid or stereo analysis: it encompasses a broader range of UHECR energies, its aperture calculation is less sensitive to atmospheric variation than the corresponding stereo calculation,[2] and its systematic uncertainties are independent of those used in the SD analysis. A monocular measurement of the energy spectrum is therefore an important complement to the same spectrum as measured by the SD array.

Two different designs of FD station are in use at TA: the northern station, Middle Drum (MD), uses refurbished hardware from the High Resolution Fly's Eye ("HiRes") cosmic-ray experiment, which collected data at Utah's Dugway Proving Ground from 1997 to 2006 [4]. MD's data acquisition (DAQ) system is based on sample-and-hold electronics, in which each pixel of a telescope's image reports a single value for signal intensity and a time reference. The southeastern and southwestern FD stations, respectively dubbed Black Rock Mesa (BRM) and Long Ridge (LR), consist of new telescopes designed for TA that use flash analog-to-digital converter (FADC)-based electronics to record the evolution of each pixel's signal intensity.

In this paper, we report the UHECR energy spectrum above 10^{18} eV as measured by the two FADC-based FDs operating in monocular mode. The corresponding measurement by the MD FD has been reported elsewhere [5], as has the energy spectrum measured by the SD array [6]. In Section 2, we elaborate on the construction and operation of the BRM and LR FDs, whose data we analyze as described in Section 3. Section 4 describes the Monte Carlo simula-

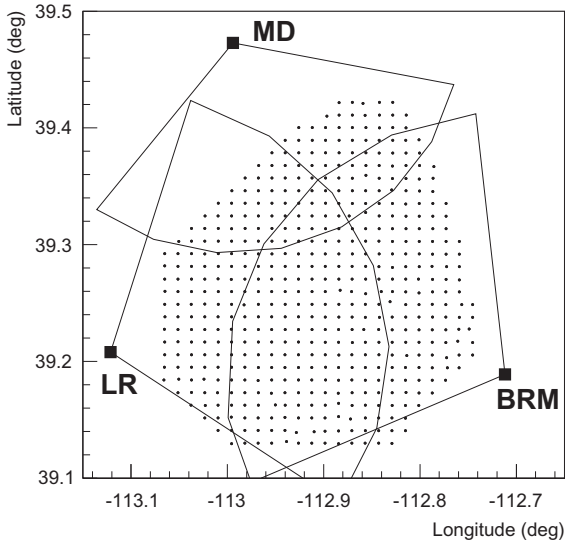

Fig. 1. The Telescope Array experiment in western Utah consists of three FDs (squares) and 507 SDs (dots). The southeastern and southwestern FDs (Black Rock Mesa and Long Ridge, respectively) use new telescopes designed for Telescope Array and based on FADC electronics; the northern FD (Middle Drum) consists of telescopes refurbished from the High Resolution Fly's Eye experiment. The FDs' approximate fields of view for 10^{19} eV cosmic rays are outlined. The average distance between neighboring SDs is 1200 m.

[1] The largest UHECR detector is the Pierre Auger Observatory in Argentina [1].

[2] The stereo aperture is the intersection of the individual FD site apertures, and has a much larger boundary-to-bulk ratio.

tion process by which we calculate the detectors' sensitivity. We present the energy-spectrum measurement in Section 5, followed by a combination of our measurement with that from the MD FD (Section 6). We conclude with a discussion of our results in Section 7. Our results are corroborated by a separate monocular analysis not described in detail here, using computer programs and processing techniques developed independently from ours [7,8].

2. FADC-based fluorescence detectors

The TA experiment's FADC-based FDs occupy two sites at the southern end of the array. The BRM FD site contains twelve telescopes with a contiguous field of view ranging from 3° to 33° in elevation in directions to the west and northwest (as shown in Fig. 1). The LR FD site is identical to BRM in its construction, but with an eastward orientation. Each telescope consists of a segmented spherical mirror 3.3 m in diameter, which focuses light from a 15-degree (elevation) by 18-degree (azimuth) region of the sky onto a cluster of 256 hexagonal photomultiplier tubes (PMTs; Hamamatsu model R9508) [9]. The PMTs are sampled by FADC electronics at an effective rate of 10 MHz with a 14-bit dynamic range, tracking the mean and variance (σ^2) over sliding time windows of 0.8, 1.6, 3.2, 6.4, and 12.8 μs. When a given PMT's instantaneous signal minus the mean in any time window exceeds six standard deviations (6σ), the trigger criterion for that PMT is met. Five or more contiguous triggered PMTs within a 25.6-μs trigger frame result in a readout of a 51.2-μs waveform from all 3072 PMTs (the trigger frame plus a 12.8-μs buffer immediately before and after) [10]. A 12.8-μs overlap between consecutive trigger frames ensures continuous detector acceptance during the frame transition. The typical trigger rate for a single FD site is approximately 2 Hz.

A typical night of FD operation is broken into several parts; each part consists of a predetermined number of triggers. Data parts may last from a few minutes to more than an hour. Parts for data collection are interspersed with parts designated for calibration purposes, which may involve reduced trigger thresholds or the use of an artificial light source that renders those parts unsuitable for data analysis. For much of the observation time reported here, the LR FD site has been operated remotely from the control room at the BRM FD site; the logistics of remote operation have resulted in a smaller duty cycle for LR than for BRM.

We assign a single numerical score to describe the weather on each night of operation based on human FD operators' logs as well as automated monitoring, and designate adjacent ranges of scores as "excellent," "good," and "bad" weather. In this analysis, we use only data from nights with good or excellent weather scores. In addition to rejecting data from nights with bad weather scores, we reject data parts that have a low rate of downward-going events whose average angular speed is less than $40^\circ\ \mu s^{-1}$. The typical rate of such events in good weather is 0.1 Hz; we reject parts with rates below 0.067 Hz. Our results include data taken from the beginning of April 2008 through mid-September 2011, representing 2020.8 hours eligible gross night-sky time for BRM and 1835.5 hours for LR. The readout of a detector following a trigger results in a brief period of insensitivity. The average "dead time" fraction for BRM and LR reduces their observing times by 7.8% and 8.7% of their respective on-times. These on-time values do not include data parts excluded from the analysis for reasons related to DAQ errors or lack of instantaneous detector calibration information.

Calibration of the FDs (described in detail elsewhere [11]) is based on the absolute calibration of a subset of PMTs, two or three per telescope, in the laboratory. A controlled quantity of 337.1-nm photons illuminate the photocathode of a PMT connected to DAQ electronics identical to those in the field, including cables of the correct length, to determine the precise relationship between electronic response and incident light [12]. To detect any long-term calibration drift, these PMTs are outfitted with a small amount of α-emitting material adjacent to a scintillator to provide a reference signal. Additionally, each telescope is equipped with a xenon flasher at the center of the mirror that illuminates that telescope's entire PMT cluster over the course of a night of observation, which enables the accurate propagation of the reference PMTs' calibration to the remainder of the cluster, as well as tracking variations in PMT gain with changing ambient temperature. The wavelength-dependent reflectance of the mirrors is measured monthly, with values interpolated for every ten-day period. Two additional wavelength-dependent quantities are assumed to be constant, the transparencies of the "BG3" UV-bandpass filter affixed to each PMT and of the Paraglas acrylic window installed as a protective cover over the entire PMT cluster. This combination of time-independent and time-dependent detector calibrations enables us to accurately interpret the recorded electronic signals in terms of incident photoelectrons with hourly time resolution during the data-analysis stage.

3. FD data analysis

Analyzing the data collected by the FDs is a process of several steps, beginning with the raw data and ending with a set of cosmic-ray events whose trajectories and air-shower longitudinal profiles satisfy quality cuts carefully chosen via Monte Carlo simulation. Steps of data reduction alternate with steps of further processing.

Our first step in data analysis is preprocessing to remove unwanted PMTs: those telescopes that are not neighbor to a triggered telescope are discarded, and those PMTs within the retained telescopes whose signal never attains a 3σ excess above the baseline are also discarded. The remaining PMTs, which consist of true "signal" PMTs as well as "noise" PMTs whose background fluctuations reached 3σ significance, are eligible for consideration in all further stages of analysis, which begins with geometry reconstruction.

Every PMT's waveform is processed by a digital signal processing algorithm that subtracts the recorded baseline level, calibrates and integrates the remaining signal (number of photoelectrons N_{pe}), and calculates the weighted average arrival time at that PMT. The shower-detector plane (SDP) is defined by the straight-line trajectory of the UHECR and a single reference point at the FD site. Each PMT i has a nominal pointing direction $\hat{v}_i$ relative to the FD site, and the SDP is determined by an iterative process to be that whose normal vector $\hat{n}$ minimizes the plane-fit χ^2 given by

$$\chi^2 = \sum_{i=1}^{N_{\rm good}} (\hat{n} \cdot \hat{v}_i)^2 N_{pe,i}, \tag{1}$$

where $N_{\rm good}$ is the number of "good" PMTs (a clustering algorithm identifies high-significance PMTs contiguous with other high-significance PMTs, as expected for emission along a line source). Fig. 2 illustrates one example of an event with the SDP calculated from the weighted PMT directions. With the SDP thus determined, the impact parameter R_p and inclination angle ψ of the shower track within the plane are related to the arrival time t_i of the signal in each PMT by the equation [13]

$$t_i = t_0 + \frac{R_p}{c} \tan\left[\frac{1}{2}(\pi - \psi - \alpha_i)\right], \tag{2}$$

where t_0 is the time of closest approach to the FD and α_i is the viewing angle of the ith PMT within the SDP relative to the direction to the shower-core impact location. The three parameters (R_p, ψ, and

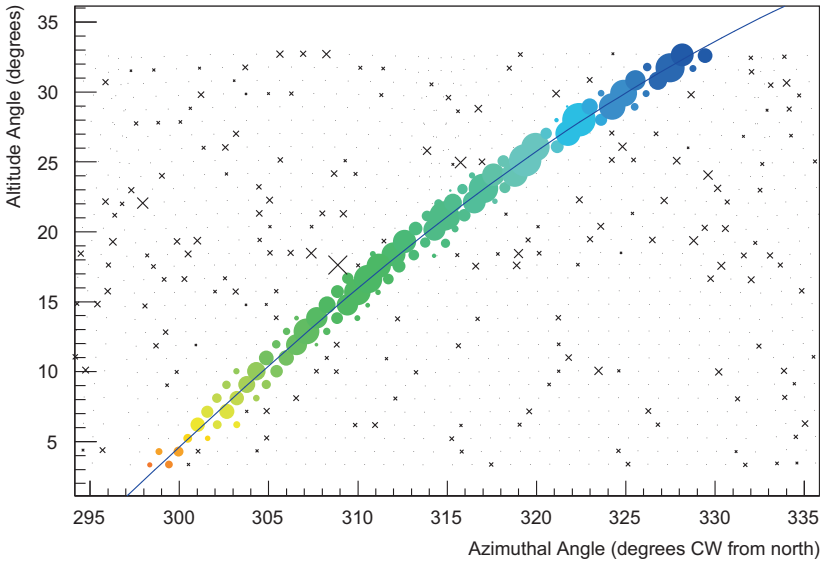

Fig. 2. The projection on the sky of the signal produced by one event in our data set. The colored circles represent "good" PMTs (those that are included in the geometry fit and subsequent Gaisser–Hillas reconstruction), where the diameter of each circle is proportional to N_{pe} and the color represents the weighted average signal time: the earliest signals are blue, with the last signals (some 13 μs later in this example) colored orange. PMTs that are designated "noise" and excluded from the reconstruction are marked with the symbol ×, and the viewing directions of PMTs discarded during raw-data preprocessing are marked with single dots. The calculated shower-detector plane (Eq. (1)) is superimposed as a solid line. (For interpretation of the references to color in this figure legend, the reader is referred to the web version of this article.)

t_0) are determined by fitting the viewing angles and signal times of good PMTs with central viewing directions not displaced more than 2° from the SDP. An air shower's Molière radius subtends less than 2° at the typical distance (> 5 km) to the showers in our data set [14], so this limit excludes predominantly "noise" PMTs far from the SDP.

Many of the events that are reconstructed in this way do not preserve enough good PMTs, or have an otherwise unfavorable geometry, for a high probability of accurate reconstruction; these events are discarded. A Monte Carlo FD simulation (described in detail in Section 4) reveals the parameter space in which the detectors' resolution (reconstruction accuracy) is optimized. We subject the reconstructed events to a series of quality cuts developed to ensure this accuracy. The cuts for monocular FD reconstruction are described in Table 1.

Those events whose geometry and signal qualify them for further processing proceed to the next stage of data analysis: shower profile reconstruction. The evolution of the number of charged particles N_e in an air shower as a function of slant depth X (traversed atmospheric column density, measured in g cm^{-2}), or shower profile, can be described on average by the Gaisser–Hillas (GH) formula [15],

$$N_e(X) = N_{\max}\left(\frac{X - X_0}{X_{\max} - X_0}\right)^{\frac{X_{\max} - X_0}{\Lambda}} \exp\left(\frac{X_{\max} - X}{\Lambda}\right). \quad (3)$$

The four GH parameters ($N_{\max}$, $X_{\max}$, X_0, and Λ) respectively represent the maximum number of charged particles in the shower, the slant depth of shower maximum, an offset in slant depth, and the characteristic interaction depth between subsequent particle generations within the shower. Because we do not typically observe the beginning or end of the shower, we are insensitive to X_0 and Λ, so we have fixed these parameters to values based on averages of fits to showers generated by the cosmic-ray simulator CORSIKA [16]: $X_0 \equiv -100$ g cm^{-2} and $\Lambda \equiv 60$ g cm^{-2}. We reconstruct the GH profile of a particular shower by simulating the detector's response to a shower with a given set of GH parameters, and varying those parameters until the best agreement between the simulated and observed time-integrated numbers of photoelectrons on a tube-by-tube level is attained.

Table 1
Cuts used to select good data after the geometry fitting stage of the Black Rock Mesa and Long Ridge monocular analysis. The "Ring-2" track-length cut applies to shower tracks that are detected in whole or in part by those telescopes with fields of view at higher elevation angles (18° to 33°).

Geometry cut		
Successful timing fit		
Good PMT fraction	⩾	3.5%
Number of good PMTs	⩾	6
N_{pe}/degree	>	25
Distance (angular speed)	>	1.5 km
SDP angle	⩽	80°
R_p	⩾	500 m
ψ fit uncertainty	<	36°
Timing fit χ^2/DOF	<	10
Track length	>	7°
(including Ring-2)	>	10°
Zenith angle	<	70°
t_0	<	25.6 μs
ψ	<	110°
Δt (duration)	>	6 μs (for $R_p < 5$ km)

To simulate the FD signal produced by an air shower, we must determine, in sequence, the amount of energy deposited into the atmosphere by the air shower, the production of light in response to that energy deposit, the attenuation of that light en route to the detector, the acceptance of light by the detector optics, and the response of the electronics to the accepted light. The atmospheric temperature, pressure, and density profiles are obtained from nightly radiosonde measurements at the Salt Lake City International Airport (SLC).[3] We first divide the trajectory into longitudinal segments of equal slant depth $\Delta X = 1$ g cm^{-2}. The value of $N_e(X)$ at the center of each segment is translated to an atmospheric energy deposit for that segment according to Nerling et al. [17]. The fluorescence yield for that energy deposit is distributed according to the spectrum measured by the FLASH collaboration [18] in bins of $\Delta\lambda = 5$ nm, with overall normalization determined by Kakimoto et al. [19]. Isotropic emission of fluorescence photons originates from

points uniformly distributed along the length of the segment, with a radial displacement distribution given by the NKG function [20,21]. In addition to fluorescence light, we calculate the production of Cherenkov radiation along the shower trajectory.

Light emitted toward the FD from the air shower will be attenuated as it traverses the atmosphere. Additionally, the atmosphere along the shower may scatter light toward the FD. We calculate the effects on radiation transport from three mechanisms: absorption by ozone, Rayleigh scattering by the molecular atmosphere via the SLC radiosonde measurements, and Mie scattering by atmospheric aerosols. In our analysis, we use an average aerosol density distribution based on *in situ* measurements at the TA site [22]. The use of an average aerosol density distribution has been shown to introduce no energy-dependent effects in event reconstruction given the generally low level of aerosols in the Utah west desert [23]. The aerosol density decreases exponentially with height over a scale length of 1 km, normalized to reproduce the median vertical aerosol optical depth (VAOD) of 0.034 at 1370 m elevation.

The FD acceptance of incident light is calculated by ray tracing. Each emitting segment along the shower track within 15° of the center of a particular telescope's field of view is simulated, with photons directed into a circle circumscribing the 3.3-m diameter mirror. Rays that are obstructed by the PMT cluster or its support structure, or which pass between mirror segments, or which reflect but do not land on the face of any PMT, are discarded. Additionally, the measured non-uniformity of the PMTs' sensitivity implies that even rays incident on a PMT's photocathode may not be accepted. The accepted light fraction is oversampled by a factor of 10 (20 in the final calculation) over the observed flux to ensure that the acceptance from faint segments is not dominated by small-number statistics.

Photoelectrons produced in the PMT photocathode by accepted light produce a signal in the DAQ system. The precise time of photoelectron arrival within a 100-ns waveform bin determines the relative distribution of the signal among that bin and its successors via the impulse response function. The signals from all of the accepted photoelectrons, as well as a background contribution inferred from the measured variance in the pre-shower FADC values (9 photoelectrons per 100 ns on average), are superimposed to produce a single simulated waveform in each PMT. The integrated signal from the simulated waveform is compared with the value of the observed event in the data.

The initial value of N_{max} for each shower's simulation is chosen using a crude estimate from the shower geometry and signal intensity, and X_{max} begins at 750 g cm^{-2}. After the initial acceptance calculation, the best-estimate number of charged particles in each track segment is calculated from the observed signal using that acceptance and the atmospheric transparency, and a GH profile is fit to the estimate. If the fit value of X_{max} changes from the simulation value by more than 50 g cm^{-2}, the acceptance is recalculated. This process may be repeated additional times until the fit X_{max} is within 50 g cm^{-2} of the value used in the most recent acceptance calculation, at which time a final acceptance calculation and fit are performed using a higher oversampling factor than the preparatory calculations.

We calculate the calorimetric energy E_{cal} of the primary UHECR by integrating the product of the fit GH profile and the ionization loss rate along the entire shower track. The "missing energy," the portion of the primary's energy going into muon and neutrino production, is added to the calorimetric energy in an amount determined by CORSIKA; the missing energy accounts for 7–10% of the total UHECR energy, E_0 [24]:

$$\frac{E_{cal}}{E_0} = -0.5717 + 0.1416 \log_{10}\frac{E_{cal}}{eV} - 0.003328\left(\log_{10}\frac{E_{cal}}{eV}\right)^2. \quad (4)$$

This formula reflects a quadratic fit to the results from a purely protonic composition, which is suitable for the energy range ($E \geqslant 10^{18}$ eV) of our present analysis [25]. A heavier composition would require a slightly larger correction.

After fitting the shower profiles, we subject the processed data to additional quality cuts, which primarily ensure that the position of X_{max} is within the FD's field of view (Table 2). The separate distributions of E_0 for cosmic-ray events seen by BRM and LR are shown in Fig. 3. Additionally, we include the distribution of events present in the final data sets of both detectors. To avoid double-counting these "stereo" events (identified by trigger times coincident within 200 μs), we assign them the geometric mean of the two FDs' independent calculations of E_0. This also avoids biasing the results in favor of one detector or the other.

4. Aperture calculation

The UHECR energy spectrum is related to each FD's data (Fig. 3) by that detector's exposure, the subset of a multidimensional phase space in which cosmic rays of a given energy are detected and pass all quality cuts. In practice, this is the product of the detector's live time and its energy-dependent aperture. The former is a straightforward calculation that subtracts dead time from the gross on-time of each detector as described in Section 2. The latter is calculated by Monte Carlo simulation.

Table 2
Cuts used to select good data after the profile fitting stage of the Black Rock Mesa and Long Ridge monocular analysis. The slant depth of shower maximum X_{max} must be "bracketed" by appearing within the observed portion of the track.

Profile cut		
Successful profile fit		
First observed depth	$\geqslant$	150 g cm^{-2}
Last observed depth	$\leqslant$	1200 g cm^{-2}
Extent of observed depth	$\geqslant$	150 g cm^{-2}
X_{max} bracketed		

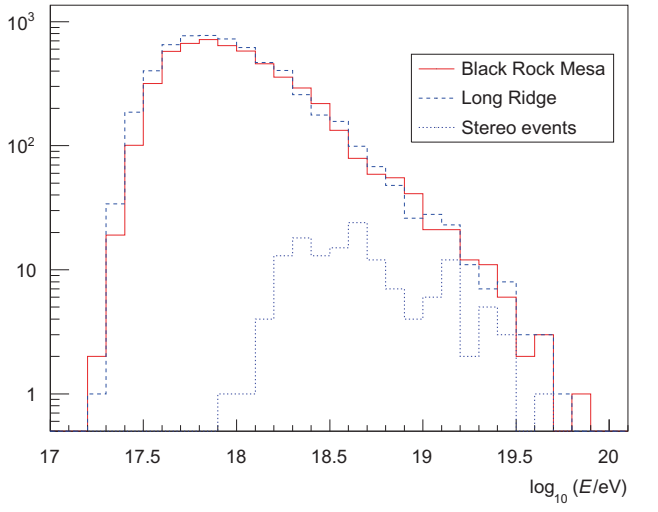

Fig. 3. The distribution of reconstructed primary energies (without cut on energy) of cosmic rays detected by Black Rock Mesa (solid red line) and Long Ridge (dashed blue line). Entries appearing in both distributions simultaneously are also shown (dotted line) by the geometric mean of their two monocular reconstructed energies. (For interpretation of the references to color in this figure legend, the reader is referred to the web version of this article.)

[3] Radiosonde profiles from two other neighboring airports—Elko Regional Airport (EKO) in Nevada and Flagstaff Pulliam Airport (FLG) in Arizona—show little variation on average from station to station [24].

To minimize distortions caused by the finite (~10%) energy resolution of monocular analysis, we simulate cosmic rays according to our best estimate of the true energy spectrum: the published HiRes spectrum [4] with a simulated proton fraction based on the composition measurements by HiRes [25] and HiRes/MIA [26]. The randomly chosen impact points for simulated showers are distributed uniformly in area over a region of Earth's surface (approximated as a sphere of radius 6370.98 km) within a radius of 1° of arc (approximately 111 km) from the center of the TA experiment. Each shower's local zenith angle is randomly selected between 0° and 80° according to an isotropic distribution. We choose the primary energy and particle type (proton or iron) according to the aforementioned previous experimental results. A library of air showers previously generated in CORSIKA and binned by energy and zenith angle for each particle species has many showers available per bin; the appropriate bin is picked, a shower is drawn at random, and its parameters are then scaled to match the desired shower properties.

Because detector calibration and atmospheric conditions vary over the period of observation represented in the data set, we simulate cosmic rays for every data part according to its duration, so that the relative contributions of all parts in simulation match those in data. We choose the mean rate of simulated showers so that the number of reconstruced Monte Carlo events passing all cuts is a few times larger than the corresponding number in the data. Given the parameter space in which we generate cosmic rays, the majority of our simulated showers do not trigger the detector electronics. Those that are determined to be incapable of doing so based on their energy and distance are simulated no further, but the rest advance to the ray-tracing simulation stage, which proceeds in the manner described in the profile-reconstruction portion of Section 3, but without oversampling the detector acceptance. If a shower triggers the detector electronics, the simulated waveforms of all 3σ PMTs (including PMTs containing night-sky background only) from the triggered telescope(s) and any neighbors are written to disk in a format identical to the preprocessed raw FD data.

The simulated-data files are then passed through the entire chain of data analysis described in Section 3. The aperture of the detector is calculated for an energy interval (width 0.1 in $\log_{10}(E/\text{eV})$) by determining the ratio of reconstructed to simulated showers in that energy interval and multiplying by the phase-space volume of simulated showers, approximately 1.18×10^5 km^2 sr. Our finite energy resolution permits showers simulated in one energy interval to be reconstructed in another, but by simulating a realistic spectrum of cosmic rays, our aperture calculation accurately models this leakage.

The respective apertures of BRM and LR have some intersection, especially at primary energies above 10^{19} eV, where showers may trigger both detectors. When combining the FD sites' individual results, the combined exposure is the sum of the sites' exposures minus their intersection. The latter is calculated using a modified version of the individual-FD Monte Carlo simulation that simulates both detectors simultaneously, and in which only reconstructed showers passing quality cuts in both detectors enter the numerator of the ratio against simulated showers (again with the geometric mean of their reconstructed energies). The detector live time for the combined exposure is the total time during which cosmic rays were simulated, reduced by an amount corresponding to the product of the live-time fractions of the two FDs (dead time at each detector is assumed to be independent for this calculation).

The separate and combined exposures, as well as the size of the subtracted intersection, are shown in Fig. 4. To reduce bin-to-bin fluctuations of statistical origin, we fit the combined exposure $\xi(E)$ with the 3-parameter function

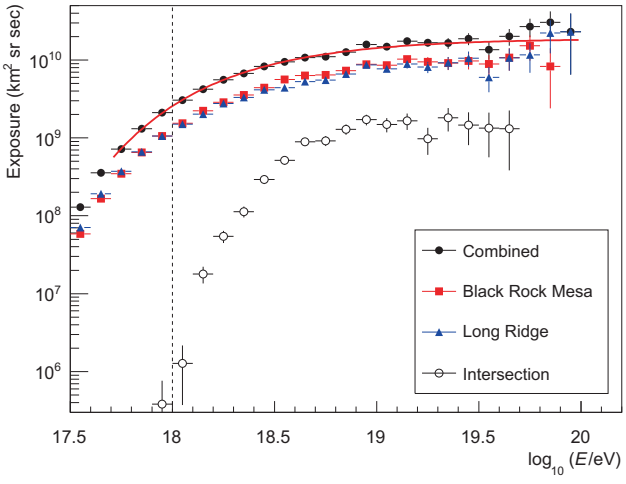

Fig. 4. The calculated exposure for Black Rock Mesa (red squares) and for Long Ridge (blue triangles). The two are summed bin-by-bin, and the intersection of the two exposures (open circles) is subtracted to calculate the combined exposure of the two detectors, which is fit to Eq. (5) (solid line). A dashed vertical line at reconstructed energy $E = 10^{18}$ eV indicates the beginning of our spectrum measurement. (For interpretation of the references to color in this figure legend, the reader is referred to the web version of this article.)

$$\log_{10}\xi(E) = p_1\left(1 - \exp\left[-\frac{\varepsilon - p_2}{p_3}\right]\right), \tag{5}$$

where $\varepsilon \equiv \log_{10}(E/\text{eV})$. The fit range, $17.7 \leqslant \varepsilon \leqslant 20.0$, begins approximately one third of a decade in energy below our minimum energy. The best-fit values of the parameters are given in Table 3.

Although our data set extends down to energies below $10^{17.5}$ eV (see Fig. 3), the aperture calculation has the least systematic uncertainty above 10^{18} eV. At lower energies, the uncertainty in the aperture grows quickly due to variations in trigger efficiency with atmospheric aerosol transparency. Additionally, the poorly known chemical composition of incoming cosmic rays introduces a systematic uncertainty that grows rapidly with decreasing energy beginning near 10^{18} eV. Consequently, we begin our spectrum measurement at 10^{18} eV, which is indicated by a vertical line in Fig. 4.

Because this exposure calculation has been performed entirely by simulation, it is necessary to verify that the simulation is an accurate representation of reality. To this end, we perform numerous data/Monte Carlo comparisons. An observable is chosen, such as the number of photoelectrons in a PMT or the shower impact parameter R_p, and the distributions of that observable in data and simulation are compared to assess the similarity in shape. A further quantitative comparison can be made by taking the ratio of the distributions and fitting it to a straight line.

In Figs. 5–7, we present a selection of data/Monte Carlo comparisons from the present analysis. Fig. 5 shows the R_p distributions broken into three broad energy bands for the BRM FD. The good agreement between the data distribution and the Monte Carlo distribution in all three bands demonstrates the proper growth of the aperture with energy. Fig. 6 shows the ψ distributions broken into

Table 3
The best-fit parameters for Eq. (5) in the range $17.7 \leqslant \varepsilon \leqslant 20.0$, fitting the exposure $\xi(E)$ (Fig. 4) in units of km^2 sr s.

Parameter	Value
p_1:	10.277 ± 0.018
p_2:	16.734 ± 0.022
p_3:	0.513 ± 0.013
χ^2/ degrees of freedom:	16.18/20

the same three energy bands, but for the LR FD. The good agreement between data and Monte Carlo demonstrates the proper angular acceptance of the aperture simulation. The complementary comparisons for each are essentially identical. Finally, Fig. 7 shows the brightness of accepted showers at BRM, which demonstrates the accurate simulation of the detector photometric threshold.

The exposure simulation's accuracy has been demonstrated by data/Monte Carlo comparison. It thus enables us to calculate our detectors' resolution in several observables. The resolutions in R_p, ψ, and N_{max} are presented in Fig. 8. In particular, the N_{max} resolution constrains the smallest physically meaningful energy interval when constructing our data and exposure histograms.

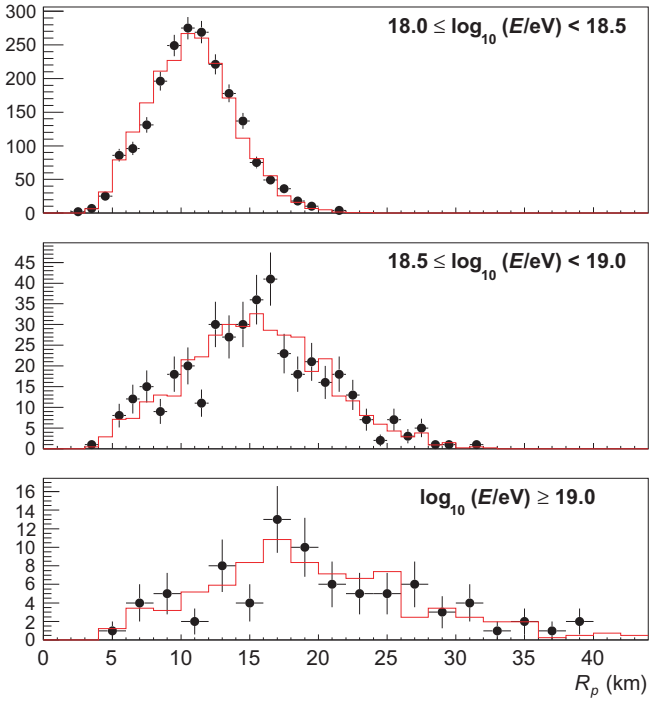

Fig. 5. Data/Monte Carlo comparison for Black Rock Mesa impact parameter R_p. The comparison is divided into three ranges of reconstructed energy. Points represent data; the histogram represents Monte Carlo.

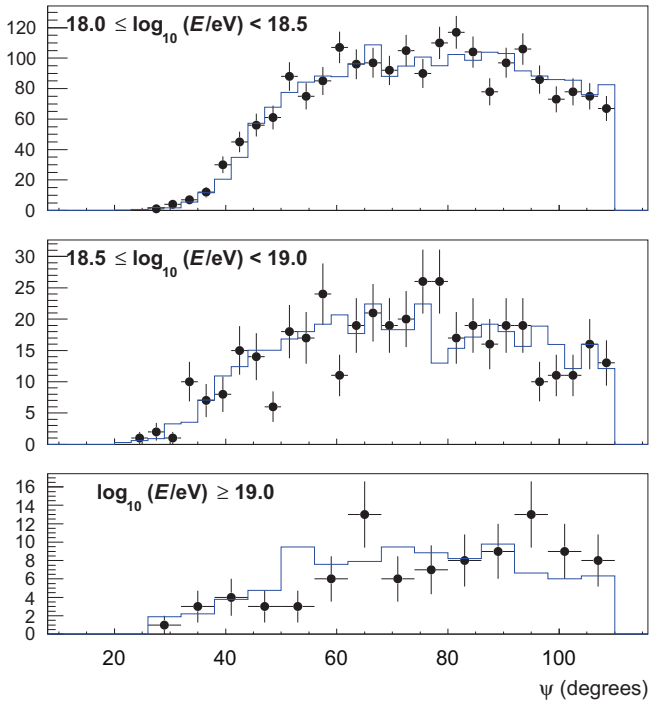

Fig. 6. Data/Monte Carlo comparison for Long Ridge shower inclination angle ψ. Points represent data; the histogram represents Monte Carlo.

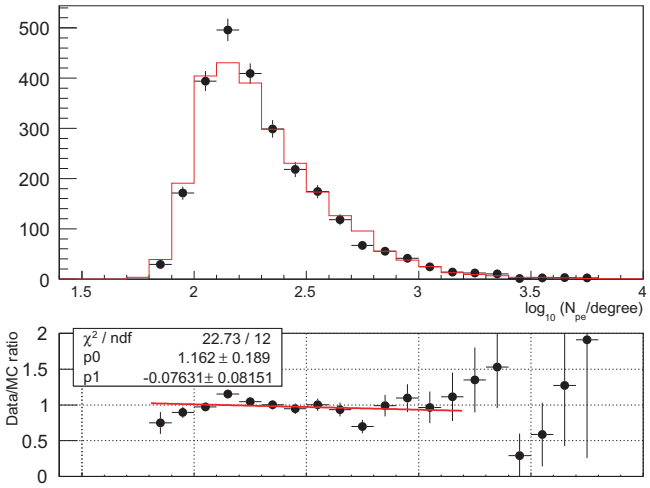

Fig. 7. Data/Monte Carlo comparison for the number of detected photoelectrons per degree of shower track at Black Rock Mesa. A linear fit to the ratio (only considering bins containing a minimum of 10 data events) reveals no significant slope. Points represent data; the histogram represents Monte Carlo.

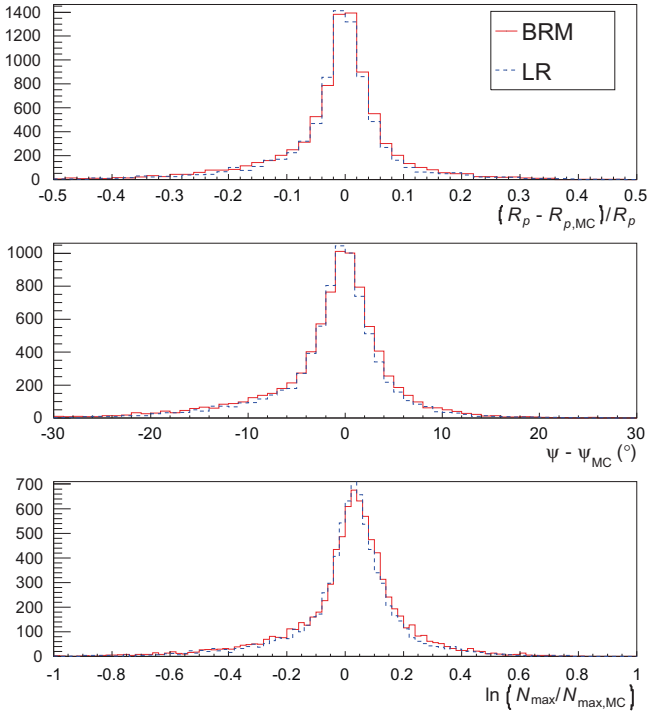

Fig. 8. The detector resolution of Black Rock Mesa (solid red lines) and Long Ridge (dashed blue lines) in two shower geometry observables (impact parameter R_p, top, and inclination angle ψ, middle) and the Gaisser–Hillas profile parameter N_{max} (bottom). The respective FWHM values are 7.7%, 5.4°, and 15.7%. (For interpretation of the references to color in this figure legend, the reader is referred to the web version of this article.)

5. Monocular FADC FD energy spectrum

The energy spectrum of the UHECR flux $J(E)$ is the ratio of the number of data events to the exposure. In the ith energy interval of width ΔE_i and where E_i is the geometric mean of the interval limits, there are n_i events, and

$$J(E_i) = \frac{n_i}{\xi(E_i)\Delta E_i}. \quad (6)$$

For clarity's sake, we have multiplied the spectrum by E^3 in Fig. 9. For comparison, we also present the published results from the MD FD and the SD ground array. Using a binned maximum-likelihood fit, we determine parameters for the twice-broken power law that best reproduces our data (Fig. 3) given our exposure (Fig. 4). These parameters appear in Table 4.

6. Combined FD monocular spectrum

To obtain a unified Telescope Array measurement of the UHECR spectrum in monocular mode, we combine our FADC-based FD result with the independent measurement performed using the MD FD [5]. To combine these measurements properly, we merge their observed UHECR data sets (an event observed by more than one detector enters the merged data set with the geometric mean of its two or three measured energies) and their respective exposures. Combining the exposures requires that we account for their intersection, which we estimate via the energy-dependent fraction of events in the MD data set seen by at least one other detector. The resulting TA FD monocular spectrum is shown in Fig. 10, with the SD spectrum [6].

7. Discussion and conclusions

The UHECR energy spectrum, as measured by TA's FADC-based FDs in monocular mode using 3.5 years of data, is shown in Fig. 9. The shape of the spectrum plot is dominated by a power-law dependence of flux on energy, punctuated by two abrupt changes in the spectral index. These breaks, a hardening of the spectrum near $10^{18.74}$ eV and a softening near $10^{19.50}$ eV, are respectively recognizable as the "ankle" and a high-energy suppression consistent with the Greisen-Zatsepin-Kuzmin (GZK) mechanism [27,28]; both

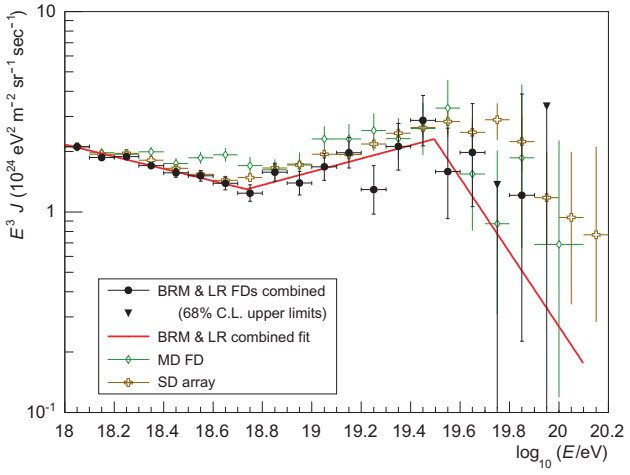

Fig. 9. The spectrum from the data and exposure of the combined Black Rock Mesa and Long Ridge FDs, with a twice-broken power-law fit (parameters given in Table 4). Included for comparison are two other spectrum measurements by Telescope Array analyses: the Middle Drum FD (green diamonds) [5], and the surface detector array (brown crosses) [6]. (For interpretation of the references to color in this figure legend, the reader is referred to the web version of this article.)

Table 4
The best-fit parameters with statistical uncertainties for the FADC monocular energy spectrum (Fig. 9) using a continuous twice-broken power-law function in the range $18.0 \leqslant \varepsilon \leqslant 20.1$.

Parameter	Value
Flux at 1 EeV (10^{-30} eV^{-1} m^{-2} sr^{-1} s^{-1}):	2.17 ± 0.05
Power below ankle:	3.30 ± 0.03
ε at ankle:	18.74 ± 0.09
Power above ankle:	2.67 ± 0.09
ε at cutoff:	19.50 ± 0.14
Power above cutoff:	4.9 ± 0.9
χ^2/ degrees of freedom:	11.92/15

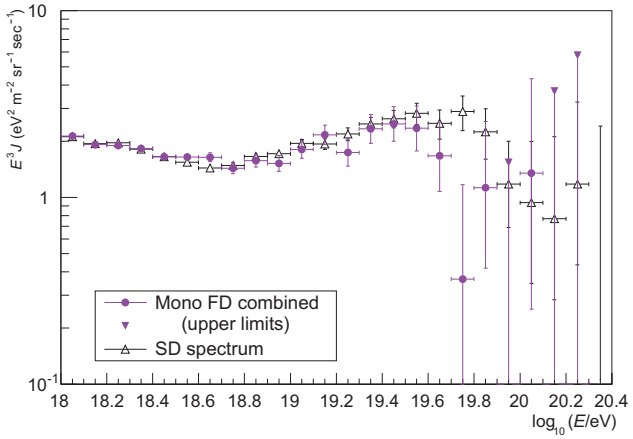

Fig. 10. The spectrum produced from the combined data and exposure of the Black Rock Mesa, Long Ridge, and Middle Drum FDs.

breaks have been present in parallel and previous measurements of the UHECR spectrum [4–6,29]. Our detection of the GZK suppression has a statistical significance of 3.2σ relative to a spectrum that continues unbroken from the ankle. We observe 5 events above $10^{19.6}$ eV, where an extension of the pre-GZK slope yields an expectation of approximately 16.88 events given the FDs' combined exposure.

The energy values at the spectral breaks are determined by our energy scale, which has a cumulative systematic uncertainty of 21%. Some of the larger contributors to this value are uncertainty in the physics models used in calculating the calorimetric energy and fluorescence yield as a function of primary energy and particle species (11%) [18], as well as the attenuation of light by the atmospheric aerosol distribution (10%; the observed RMS of the VAOD distribution is 0.015, compared to the median value of 0.034 [22]). The absolute photometric calibration of the detectors contributes another 11% systematic uncertainty to the energy measurement [12,24]. Given the power-law nature of the spectrum, the 21% systematic uncertainty on the energy results in an uncertainty on the measured UHECR flux of 35%. The effect of changing aperture combined with our systematic energy uncertainty of 21% is less than 35% at all energies greater than 10^{18} eV. In Fig. 9, the spectrum measurement from the FADC-based FDs is indeed systematically lower than the spectra from the MD FD and the SD array, but the difference is within our systematic uncertainty.[4]

Acknowledgments

The Telescope Array experiment is supported by the Japan Society for the Promotion of Science through Grants-in-Aid for Scientific Research on Specially Promoted Research (21000002) "Extreme Phenomena in the Universe Explored by Highest Energy

Cosmic Rays," and the Inter-University Research Program of the Institute for Cosmic Ray Research; by the US National Science Foundation awards PHY-0307098, PHY-0601915, PHY-0703893, PHY-0758342, PHY-0848320, PHY-1069280, and PHY-1069286 (Utah) and PHY-0649681 (Rutgers), and through TeraGrid resources provided by Purdue University and Indiana University [30]; by the National Research Foundation of Korea (2006-0050031, 2007-0056005, 2007-0093860, 2010-0011378, 2010-0028071, R32-10130); by the Russian Academy of Sciences, RFBR Grants 10-02-01406a and 11-02-01528a (INR), IISN project No. 4.4509.10, and Belgian Science Policy under IUAP VI/11 (ULB). The foundations of Dr. Ezekiel R. and Edna Wattis Dumke, Willard L. Eccles, and George S. and Dolores Doré Eccles all helped with generous donations. The State of Utah supported the project through its Economic Development Board, and the University of Utah through the Office of the Vice President for Research. The experimental site became available through the cooperation of the Utah School and Institutional Trust Lands Administration (SITLA), the US Bureau of Land Management, and the US Air Force. We also wish to thank the people and the officials of Millard County, Utah, for their steadfast and warm support. We gratefully acknowledge the contributions from the technical staffs of our home institutions as well as the University of Utah Center for High Performance Computing (CHPC).

References

[1] J. Abraham et al., Properties and performance of the prototype instrument for the Pierre Auger Observatory, Nuclear Instruments and Methods in Physics Research A 523 (2004) 50–95, http://dx.doi.org/10.1016/j.nima.2003.12.012.
[2] K. Kasahara et al., Status and prospect of Telescope Array (TA) experiment, in: International Cosmic Ray Conference, 30th ICRC (Mérida), vol. 4, 2008, pp. 417–420.
[3] J. Matthews et al., Overview of the Telescope Array experiment, in: Proceedings of the 31st ICRC (Łódź), 2009, p. icrc1386.
[4] R.U. Abbasi et al., First observation of the Greisen–Zatsepin–Kuzmin suppression, Physical Review Letters 100 (10) (2008) 101101, http://dx.doi.org/10.1103/PhysRevLett.100.101101. Available from: <arXiv:astro-ph/0703099>.
[5] T. Abu-Zayyad et al., The energy spectrum of Telescope Array's Middle Drum detector and the direct comparison to the High Resolution Fly's Eye experiment, Astroparticle Physics 39 (2012) 109–119, http://dx.doi.org/10.1016/j.astropartphys.2012.05.012. Available from: <arXiv:1202.5141>.
[6] T. Abu-Zayyad et al., The cosmic-ray energy spectrum observed with the surface detector of the Telescope Array experiment, ApJl 768 (2013) L1, http://dx.doi.org/10.1088/2041-8205/768/1/L1. Available from: <arXiv:1205.5067>.
[7] T. Fujii, Energy spectrum of UHECRs measured by newly constructed fluorescence detectors in Telescope Array experiment, in: Proceedings of the International Symposium on Very High Energy Cosmic Ray Interactions, Berlin, 2012.
[8] T. Fujii, Measurements of the energy spectrum and the mass composition of ultra-high energy cosmic rays with Telescope Array fluorescence detectors in monocular mode, Ph.D. Thesis, Osaka City University, 2012.
[9] H. Tokuno et al., New air fluorescence detectors employed in the Telescope Array experiment, Nuclear Instruments and Methods in Physics Research A 676 (2012) 54–65, http://dx.doi.org/10.1016/j.nima.2012.02.044. Available from: <arXiv:1201.0002>.
[10] Y. Tameda et al., Trigger electronics of the new fluorescence detectors of the Telescope Array experiment, Nuclear Instruments and Methods in Physics Research A 609 (2009) 227–234, http://dx.doi.org/10.1016/j.nima.2009.07.093.
[11] H. Tokuno et al., On site calibration for new fluorescence detectors of the Telescope Array experiment, Nuclear Instruments and Methods in Physics Research A 601 (2009) 364–371, http://dx.doi.org/10.1016/j.nima.2008.12.210.
[12] S. Kawana et al., Calibration of photomultiplier tubes for the fluorescence detector of Telescope Array experiment using a Rayleigh scattered laser beam, Nuclear Instruments and Methods in Physics Research A 681 (2012) 68–77, http://dx.doi.org/10.1016/j.nima.2012.03.011. Available from: <arXiv:1202.1934>.
[13] R.M. Baltrusaitis et al., The Utah Fly's Eye detector, Nuclear Instruments and Methods in Physics Research A 240 (1985) 410–428, http://dx.doi.org/10.1016/0168-9002(85)90658-8.
[14] J. Beringer et al., Review of particle physics, Physical Review D 86 (1) (2012) 010001, http://dx.doi.org/10.1103/PhysRevD.86.010001.
[15] T.K. Gaisser, A.M. Hillas, Reliability of the method of constant intensity cuts for reconstructing the average development of vertical showers, in: International Cosmic Ray Conference, 15th ICRC (Plovdiv), vol. 8, 1977, pp. 353–357.
[16] D. Heck, J. Knapp, J.N. Capdevielle, G. Schatz, T. Thouw, CORSIKA: A Monte Carlo Code to Simulate Extensive Air Showers, 1998.
[17] F. Nerling, J. Blümer, R. Engel, M. Risse, Universality of electron distributions in high-energy air showers – description of Cherenkov light production, Astroparticle Physics 24 (2006) 421–437, http://dx.doi.org/10.1016/j.astropartphys.2005.09.002. Available from: <arXiv:astro-ph/0506729>.
[18] R. Abbasi et al., Air fluorescence measurements in the spectral range 300–420 nm using a 28.5 GeV electron beam, Astroparticle Physics 29 (2008) 77–86, http://dx.doi.org/10.1016/j.astropartphys.2007.11.010. Available from: <arXiv:0708.3116>.
[19] F. Kakimoto et al., A measurement of the air fluorescence yield, Nuclear Instruments and Methods in Physics Research A 372 (1996) 527–533, http://dx.doi.org/10.1016/0168-9002(95)01423-3.
[20] K. Kamata, J. Nishimura, The lateral and the angular structure functions of electron showers, Progress of Theoretical Physics Supplement 6 (1958) 93–155, http://dx.doi.org/10.1143/PTPS.6.93.
[21] K. Greisen, The extensive air showers, in: J.G. Wilson (Ed.), Progress in Cosmic Ray Physics, vol. 3, North Holland, 1956. pp. 3–141 (Ch. 1).
[22] T. Tomida et al., The atmospheric transparency measured with a LIDAR system at the Telescope Array experiment, Nuclear Instruments and Methods in Physics Research A 654 (2011) 653–660, http://dx.doi.org/10.1016/j.nima.2011.07.012. Available from: <arXiv:1109.1196>.
[23] R.U. Abbasi et al., Studies of systematic uncertainties in the estimation of the monocular aperture of the HiRes experiment, Astroparticle Physics 27 (2007) 370–381, http://dx.doi.org/10.1016/j.astropartphys.2006.12.004. Available from: <arXiv:astro-ph/0607094>.
[24] S.R. Stratton, Measurement of the flux of ultra-high energy cosmic rays by the Telescope Array FADC fluorescence detectors, Ph.D. Thesis, Rutgers, The State University of New Jersey, 2012.
[25] R.U. Abbasi et al., Indications of proton-dominated cosmic-ray composition above 1.6 EeV, Physical Review Letters 104 (16) (2010) 161101, http://dx.doi.org/10.1103/PhysRevLett.104.161101. Available from: <arXiv:0910.4184> .
[26] T. Abu-Zayyad et al., Measurement of the Cosmic-Ray Energy Spectrum and Composition from 10^{17} to $10^{18.3}$ eV Using a Hybrid Technique, ApJ 557 (2001) 686–699, http://dx.doi.org/10.1086/322240. Available from: <arXiv:astro-ph/0010652>.
[27] K. Greisen, End to the cosmic-ray spectrum?, Physical Review Letters 16 (1966) 748–750, http://dxdoi.org/10.1103/PhysRevLett.16.748.
[28] G.T. Zatsepin, V.A. Kuz'min, Upper limit of the spectrum of cosmic rays, Soviet Journal of Experimental and Theoretical Physics Letters 4 (1966) 78.
[29] J. Abraham et al., Observation of the suppression of the flux of cosmic rays above 4×10^{19} eV, Physical Review Letters 101 (6) (2008) 061101, http://dx.doi.org/10.1103/PhysRevLett.101.061101. Available from: <arXiv:0806.4302>.
[30] C. Catlett et al., TeraGrid: Analysis of Organization, System Architecture, and Middleware Enabling New Types of Applications, IOS Press, 2007.

[4] The MD FD systematic uncertainties (17% energy scale, 30% flux) are largely independent of those for the FADC FDs, having only the fluorescence-yield uncertainty in common.